

Electronic Supplementary Information

Multi-layer core-shell metal oxide/nitride/carbon and its high-rate electroreduction of nitrate to ammonia

Xiaoyu Li,^{a‡} Ping Deng,^{a‡} Mengqiu Xu,^{a‡} Zhenbo Peng,^b Yuhu Zhou,^a Gan Jia,^a Wei Ye,^{*a} Peng Gao^{*a} and Wei Wang^{*a}

^a College of Material, Chemistry and Chemical Engineering, Key Laboratory of Organosilicon Chemistry and Material Technology, Ministry of Education, Hangzhou Normal University, Hangzhou 311121, China.

^b Zhejiang Collaborative Innovation Center for High Value Utilization of Byproducts from Ethylene Project, Ningbo Polytechnic, Ningbo 315800, China

* Corresponding author (E-mail: yewei@hznu.edu.cn, gaopeng@hrbeu.edu.cn, wangwei2022@hznu.edu.cn)

‡ These authors contributed equally to this work.

Experimental section

Materials

Ferrous chloride ($\text{FeCl}_2 \cdot 4\text{H}_2\text{O}$, 99.5%), molybdenum pentachloride (MoCl_5 99.5%), isopropyl alcohol ($\text{C}_3\text{H}_8\text{O}$, 99.9%), nitrilotriacetic acid ($\text{N}(\text{CH}_2\text{COOH})_3$, 99.5%), ethanol (EtOH, 99.7%), ^{15}N -labeled potassium nitrate (K^{15}NO_3 , $\geq 99.5\%$), potassium nitrate (KNO_3 , A. R.), potassium hydroxide (KOH, A. R.), ultra-high purity Ar (99.999%), Nessler reagent, Griess reagent and Nafion (5 wt.%) were purchased from Sinopharm Chemical Reagent Co. Ltd. (Shanghai, China). All chemicals were used without further purification. All aqueous solutions were prepared using deionized (DI) water with a resistivity of $18.25 \text{ M}\Omega \cdot \text{cm}^{-1}$.

Characterization

X-ray powder diffraction (XRD): X-ray powder diffraction (XRD) test used a Cu-K α radiation source with a wavelength of $\lambda = 0.15405 \text{ nm}$. Voltage and current in the process of testing were 40 kV and 150 mA, respectively. The scanning speed was $5^\circ/\text{min}$ and the scanning area was from 20° to 70° .

The field emission scanning electron microscopy (FE-SEM): The field emission scanning electron microscopy (FE-SEM) images equipped with energy dispersive X-ray spectrum (EDS) was taken on a SU8000 cold emission field scanning electron microanalyzer (Hitachi, Japan).

Fourier transform infrared (FT-IR): Fourier transform infrared (FT-IR) spectra of the products were recorded on a Perkin-Elmer 580B IR spectrophotometer using the KBr pellet technique.

Brunauer Emmett Teller (BET): N_2 adsorption/desorption examinations were conducted with a Micromeritics TriStar 3020 to characterize the Brunauer-Emmett-Teller (BET) ratio of the sample. The test temperature was -196.15°C (liquid nitrogen temperature), and the samples were heated at 120°C for 2 h before the test.

Raman spectrum: Raman spectra were taken using a Raman spectrometer (LABRAM HR800) with a 667 nm laser excitation.

X-ray photoelectron spectroscopy (XPS): X-ray photoelectron spectroscopy (XPS) was used to characterize the atomic composition content and the chemical valence state, which was equipped with an excitation source of 1486.6 eV of AlK α target.

Electrochemical impedance spectroscopy (EIS): EIS experiments analysis is performed using a three-electrode system in a 0.5 M Na_2SO_4 solution using a three-electrode system, Pt foil, and saturated Ag/AgCl as the counter electrode and reference electrode by an electrochemical workstation CHI 660D (Chen Hua, China). Carrier

density calculation formula is as follows:

$$N_d = \frac{2}{e_0 \epsilon \epsilon_0} \frac{d(\frac{1}{c^2})}{dV}$$

Inductively coupled plasma mass spectrometry (ICP–MS): The concentrations of Fe were measured with a Thermo Scientific Plasma Quad 3 inductively coupled plasma mass spectrometry (ICP–MS) after dissolving the samples with a mixture of HCl and HNO₃ (3:1, volume ratio).

XAFS characterization: Fe K–edge XAFS measurements were performed at the beamline 14W1 in Shanghai Synchrotron Radiation Facility (SSRF), China. The X–ray was monochromatized by a double–crystal Si (111) monochromator. The storage ring of SSRF was operated at 3.5 GeV with the current of 300 mA. The acquired extended XAFS (EXAFS) data were processed according to the standard procedures using the WinXAS 3.1 program.

Calculation of NH₃ yield rate

$$R = (c_{\text{NH}_3} \times V) / (m \times t) \quad (1)$$

where R is the NH₃ yield rate ($\text{mol}_{\text{NH}_3} \cdot \text{g}_{\text{cat}}^{-1} \cdot \text{h}^{-1}$), c is the measured concentration (mol L^{-1}), V is the volume of the electrolyte (L), m is the mass of the catalyst on the electrode (g), and t is the reaction time (h).

$$R = (c_{\text{NH}_3} \times V) / (S \times t) \quad (2)$$

where R is the NH₃ yield rate ($\text{mmol cm}^{-2} \text{ h}^{-1}$), C is the measured concentration (mol L^{-1}), V is the volume of the electrolyte (L), S is the effective area of the electrode (cm^{-2}), and t is the reaction time (h).

Calculation of NO₃⁻-to-NH₃ FE

Faradaic efficiency (FE) was calculated by dividing the charge used for the given product by the total charge consumption (Q):

For NO₃⁻-to-NH₃:

$$\text{FE} = (8 \times F \times c_{\text{NH}_3} \times V) / Q \times 100\% \quad (3)$$

For NO₃⁻-to-NO₂⁻:

$$\text{FE} = (2 \times F \times c_{\text{NO}_2^-} \times V) / Q \times 100\% \quad (4)$$

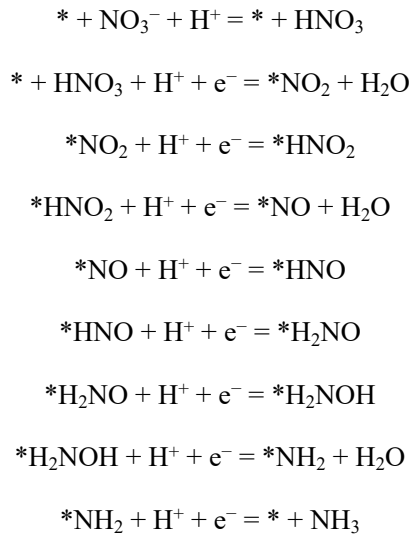
For H₂O-to-H₂:

$$\text{FE} = (2 \times F \times V_{\text{H}_2} / V_m) / Q \times 100\% \quad (5)$$

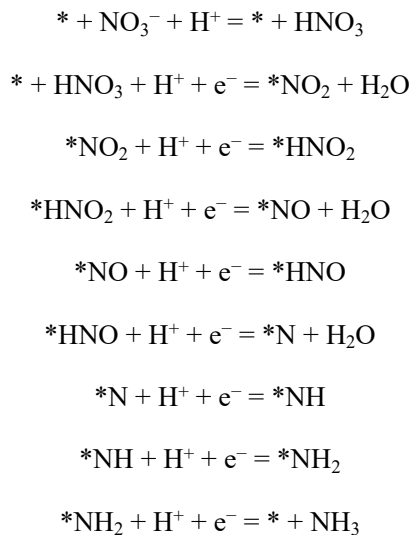
where F is the Faradaic constant ($96\,485 \text{ C mol}^{-1}$), c is the measured concentration (mol L^{-1}), V is the volume of the electrolyte (L), V_{H_2} is the volume of produced H₂ (L), and V_m is molar volume of gas in the standard state (22.4 L mol^{-1}).

Possible reaction path of NO₃RR reported in literatures¹⁻⁴

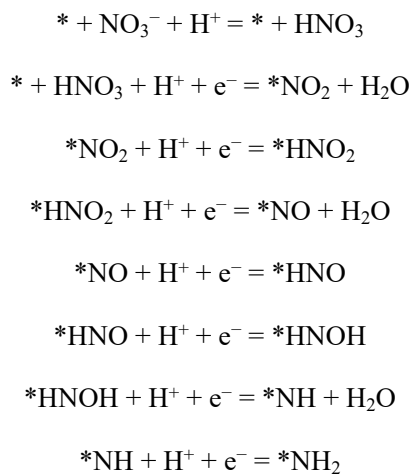
Path 1:

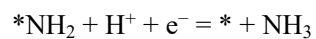


Path 2:

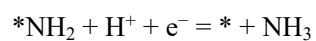
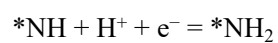
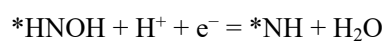
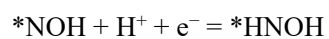
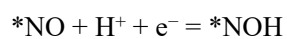
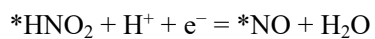
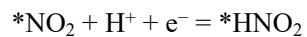
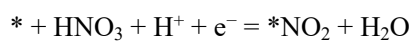
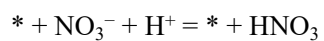


Path 3:

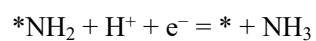
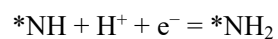
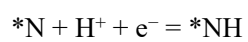
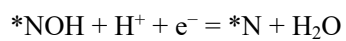
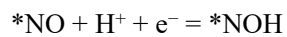
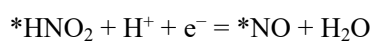
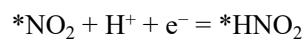
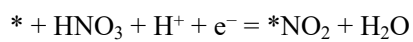
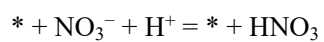




Path 4:



Path 5:



Supplementary Figures.

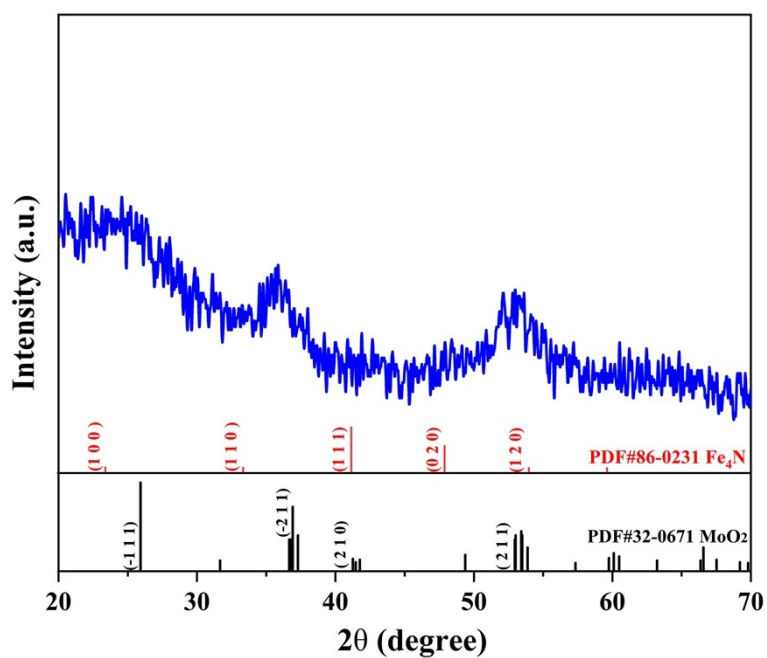


Figure S1. XRD pattern of MFN-2 precursor.

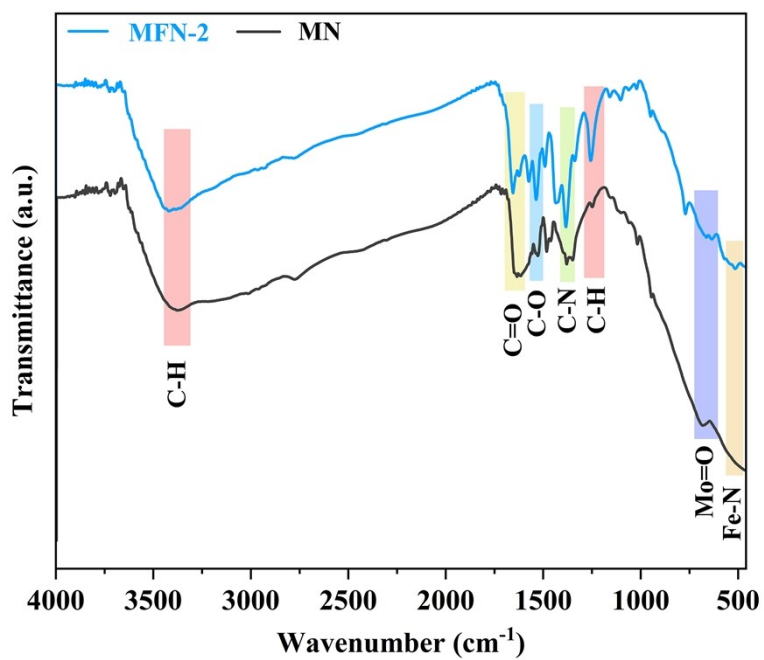


Figure S2. Fourier transform infrared spectroscopy of the precursors of MFN-2 and MN.

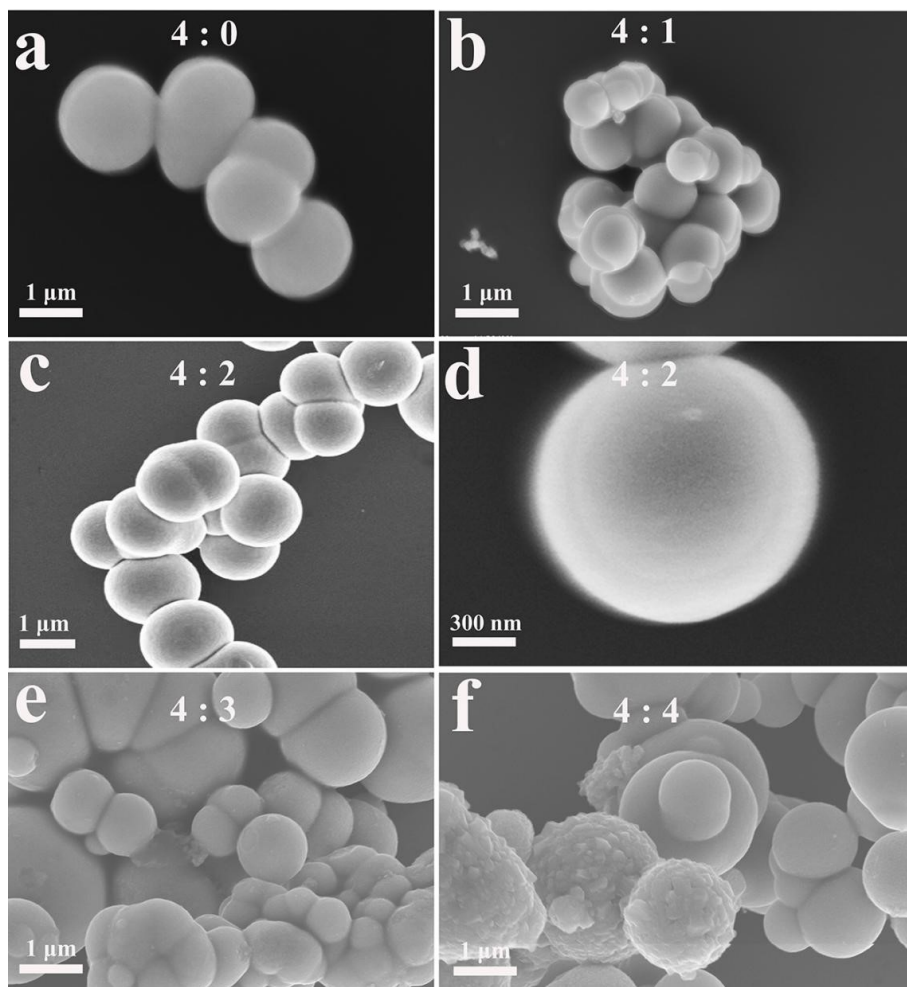


Figure S3. FE-SEM images of the precursors of (a) MC, (b) MFC-1, (c) MFC-2, (d) MFC-3 and (e) MFC-4.

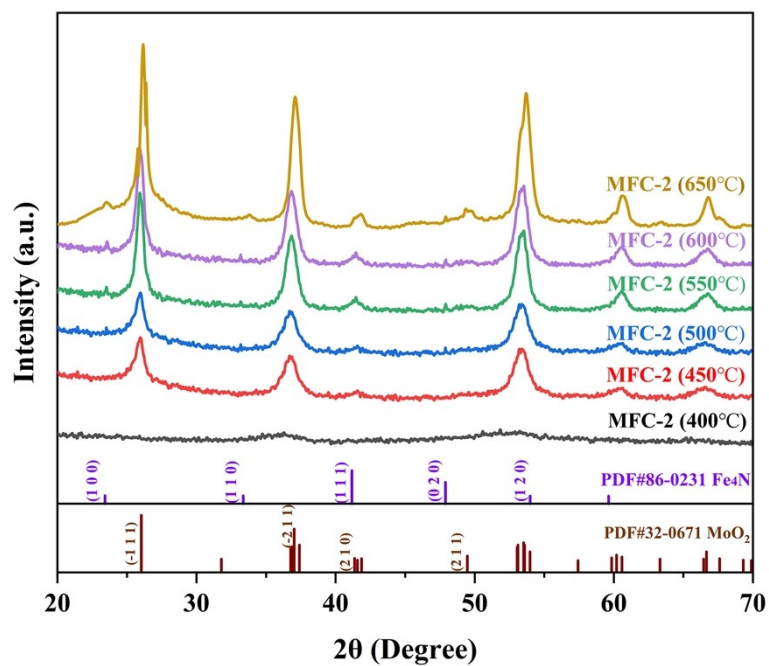


Figure S4. XRD patterns of MFN-2 samples sintered at different temperatures.

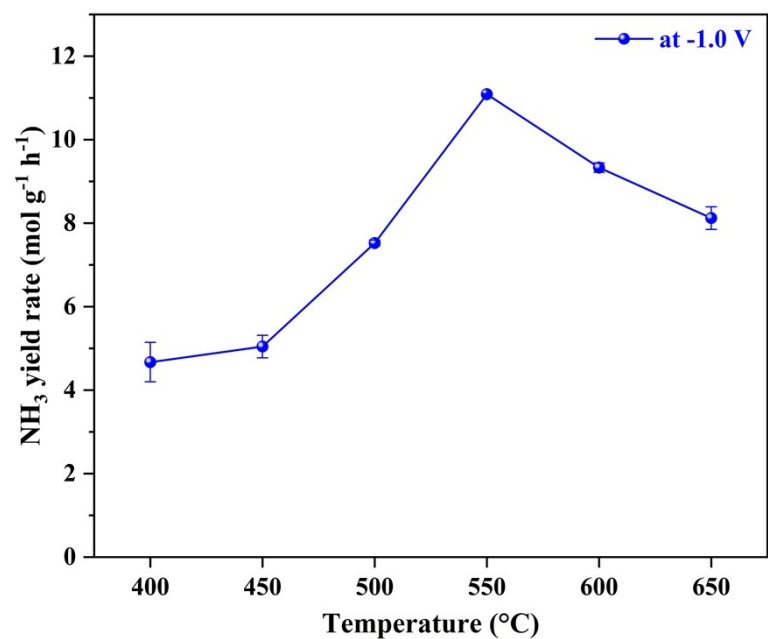


Figure S5. The corresponding ammonia yields of the samples through MFN-2 calcinating at different temperatures.

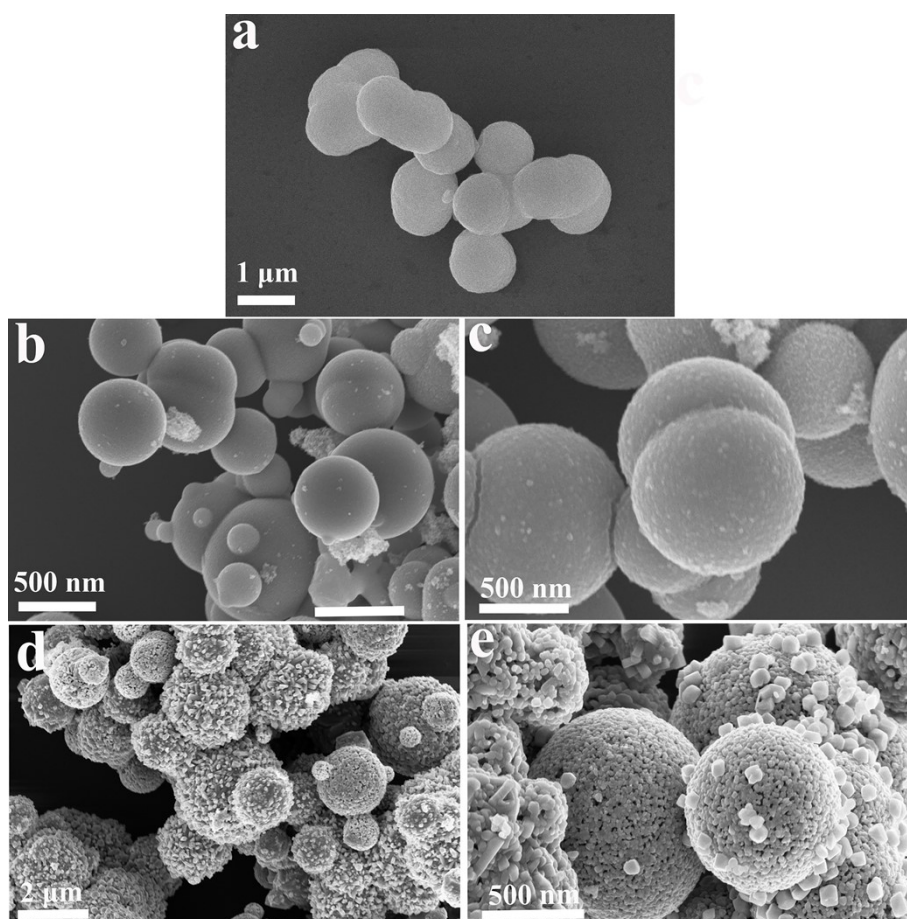


Figure S6. FE-SEM images of (a) MC, (b) MFC-1, (c) MFC-2, (d) MFC-3 and (e) MFC-4.

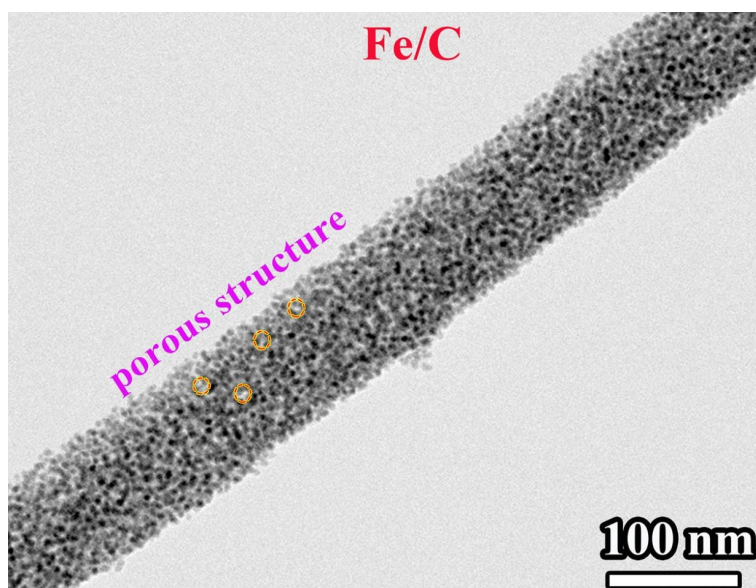


Figure S7. TEM image of the Fe/C sample prepared through Fe-NTA sintering at 550 °C.

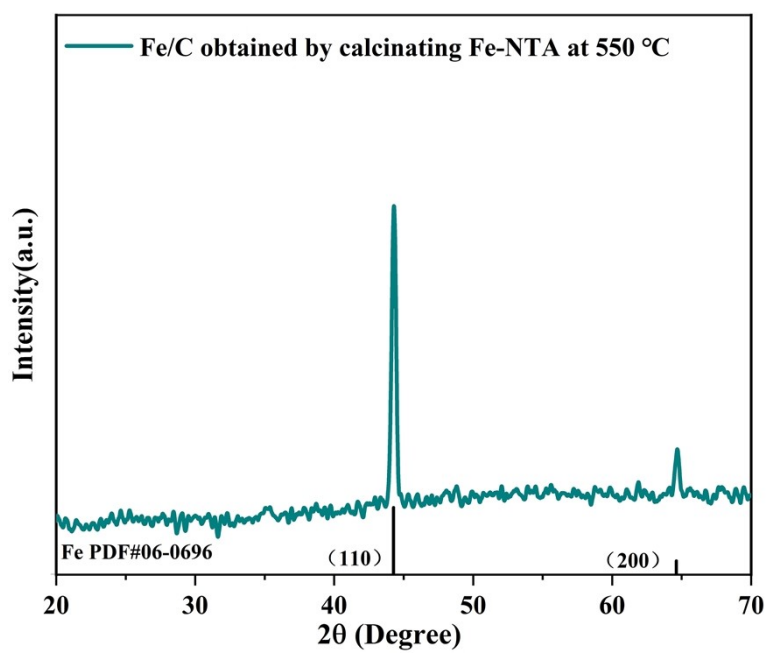


Figure S8. XRD pattern of the Fe/C sample.

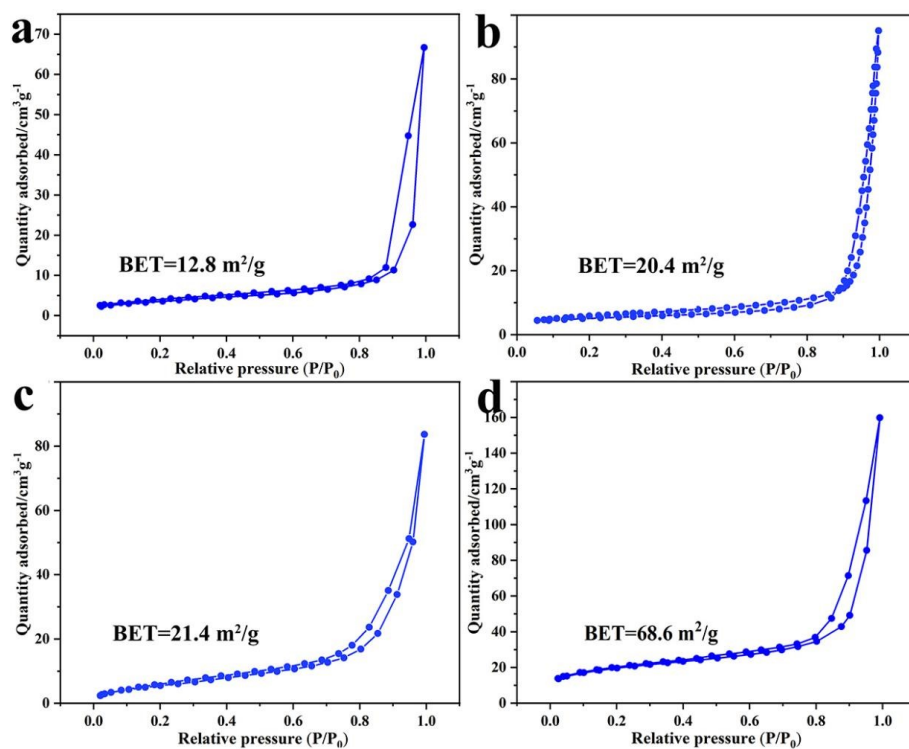


Figure S9. The N_2 adsorption/desorption curves of (a) MC and (b) MFC-1, (c) MFC-3, (d) MFC-4 respectively.

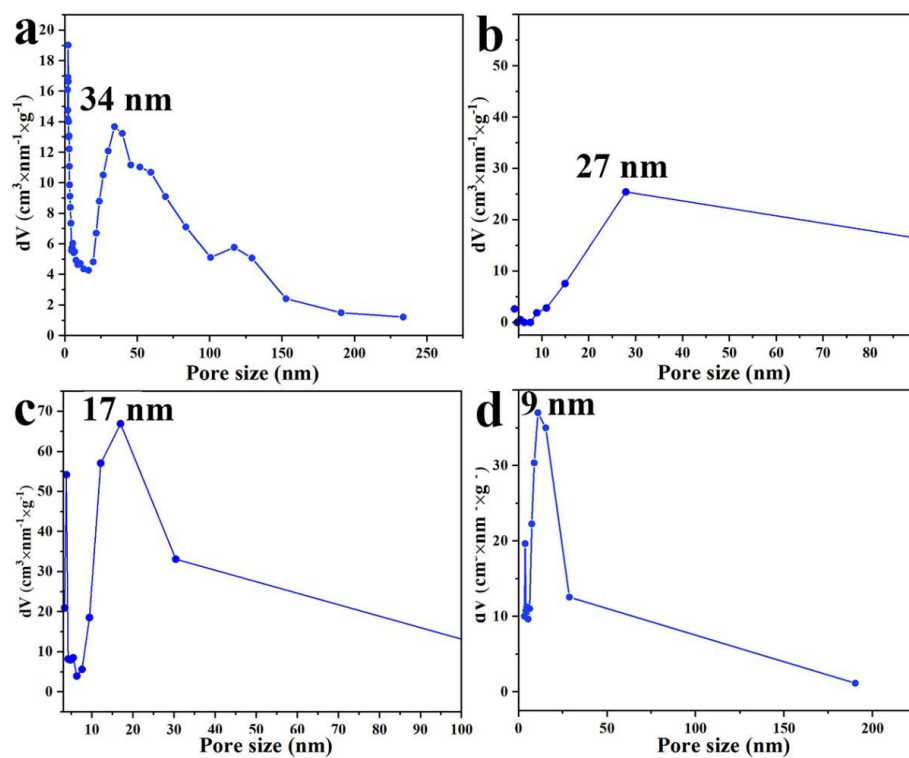


Figure S10. The pore diameter distribution curves of (a) MC and (b) MFC-1, (c) MFC-3, (d) MFC-4 respectively.

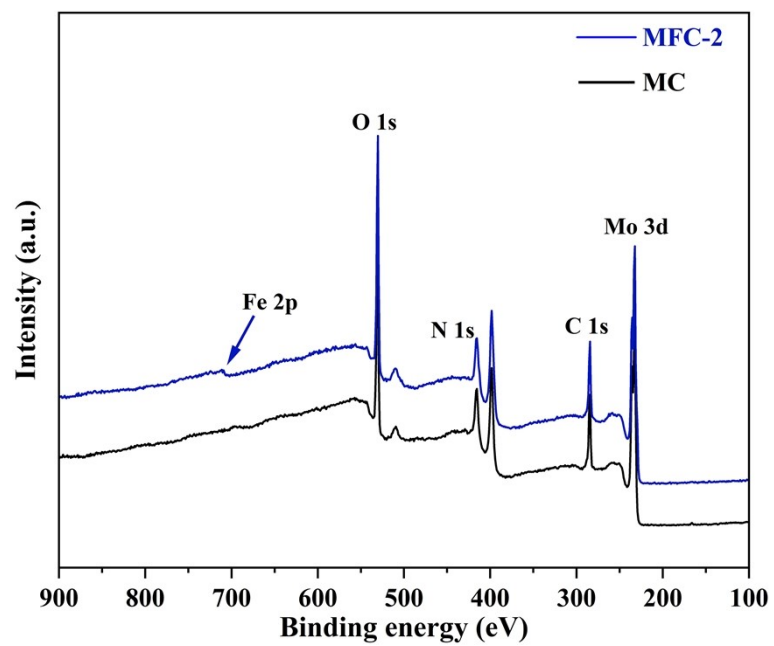


Figure S11. XPS Survey spectra of MC and MFC-2.

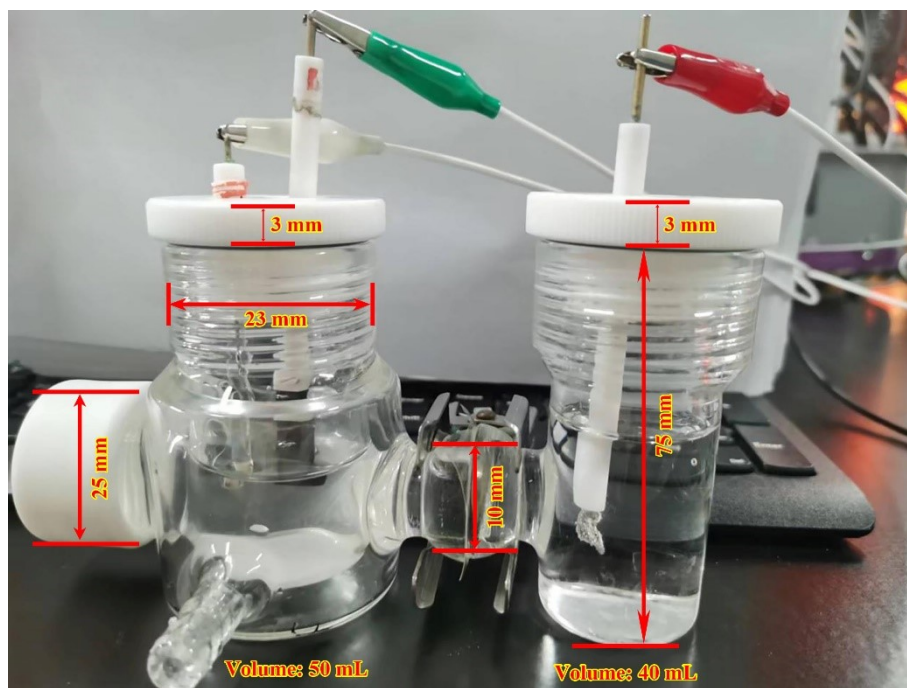


Figure S12. The picture of H-type electrolytic cell.

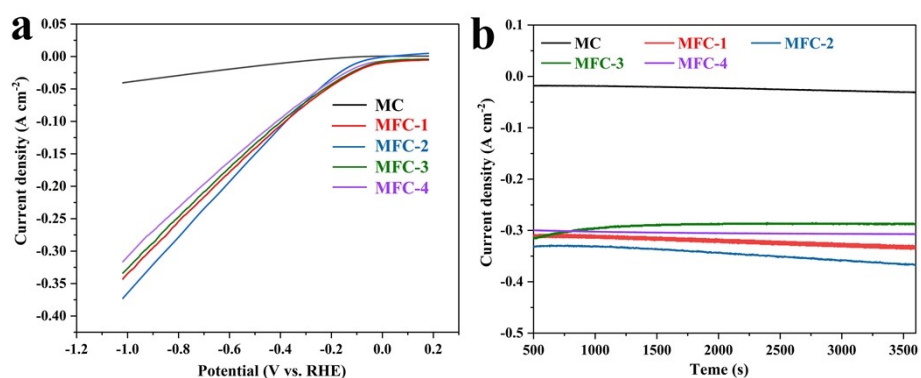


Figure S13. (a) LSV curves of MC and MFC-2 in 1 M KNO₃ and 1 M KOH electrolyte; (b) I-T curves of MC and MFC-2 in 1M KNO₃ + 1M KOH electrolyte at -1.0 V.

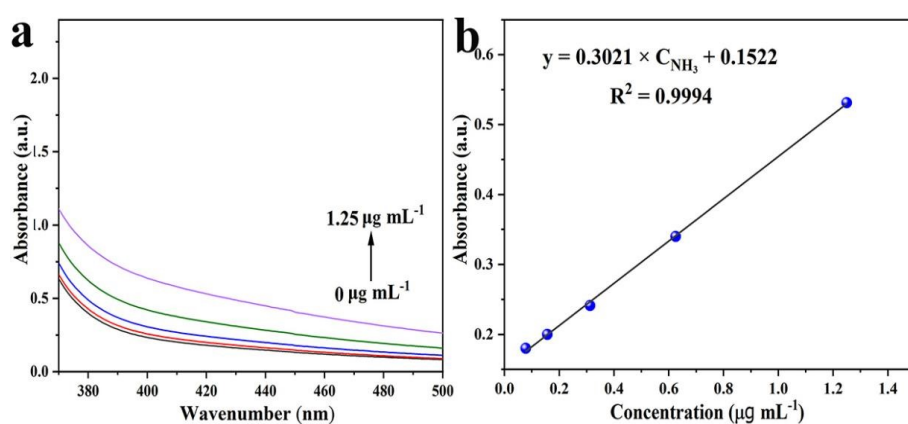


Figure S14. (a) UV-vis absorption spectra based on colorimetric method of Nessler reagent and (b) NH₄⁺ concentration-absorbance curve of standard NH₄⁺ solution with a series of concentrations.

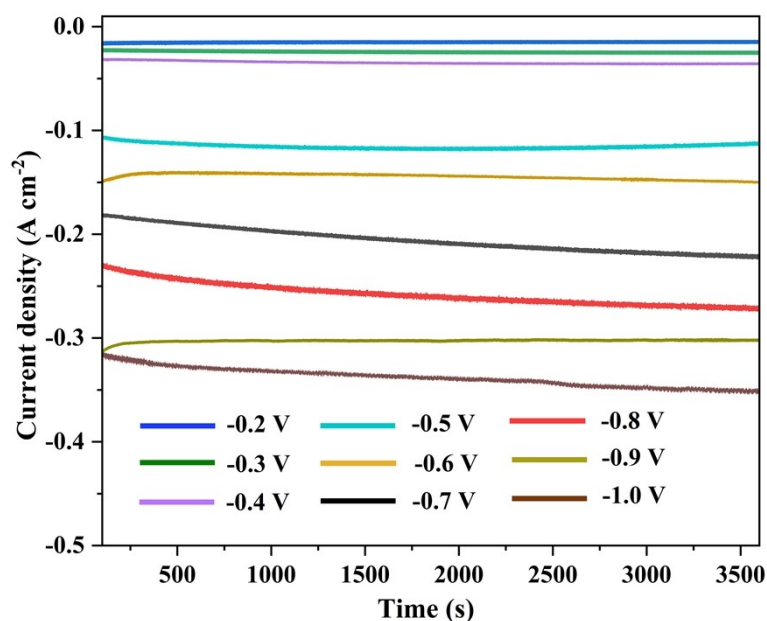


Figure S15. i-t curves of MFC-2 recorded in 1 M KNO₃ + 1 M KOH solution at the given potentials.

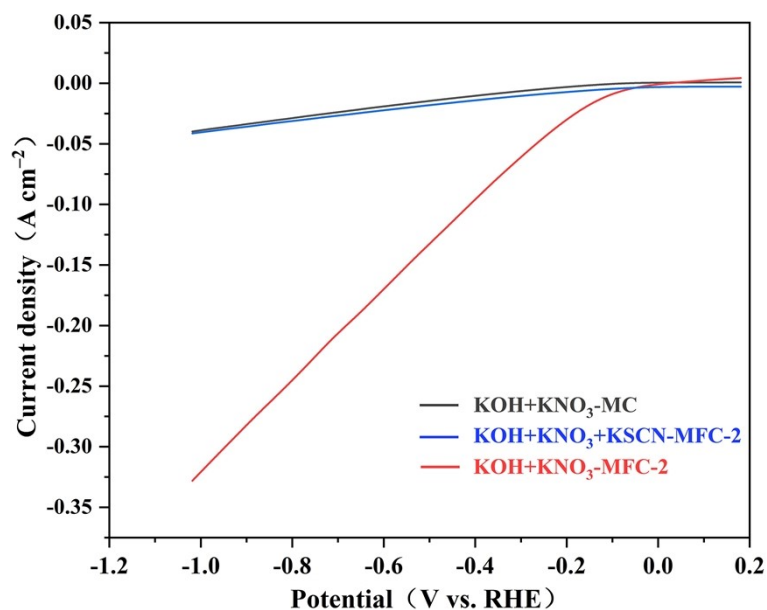


Figure S16. LSV curves of MFC-2 and MC in 1 M KNO_3 + 1 M KOH and/without 1M KSCN electrolyte.

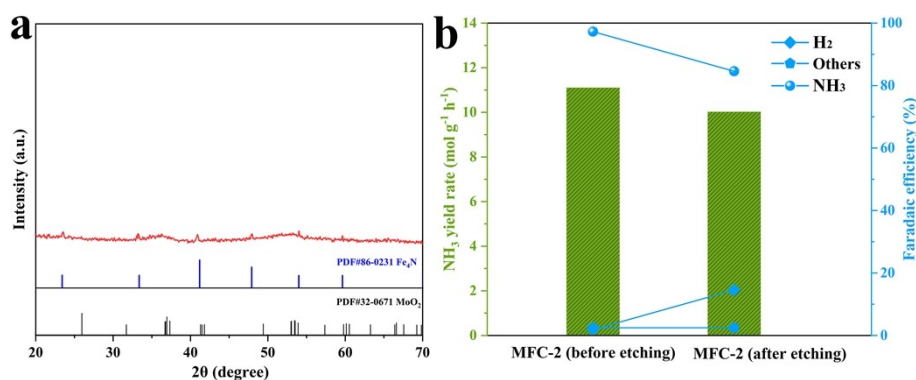


Figure S17. (a) XRD pattern and (b) the corresponding ammonia yield and Faradaic efficiency of the $\text{Fe}_4\text{N/C}$ through MFC-2 etching by 5 M KOH.

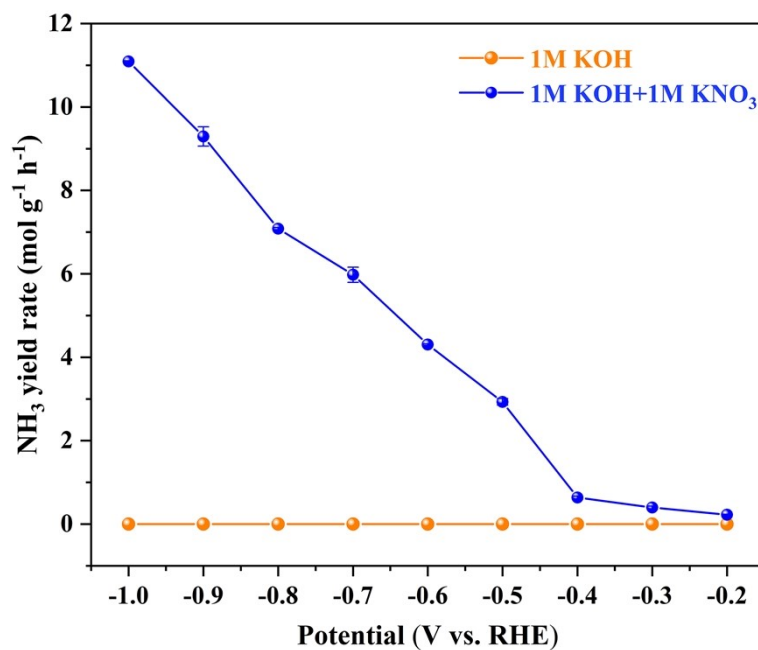


Figure S18. Ammonia yields of MFC-2 in 1 M KNO_3 + 1 M KOH and 1 M KOH electrolyte.

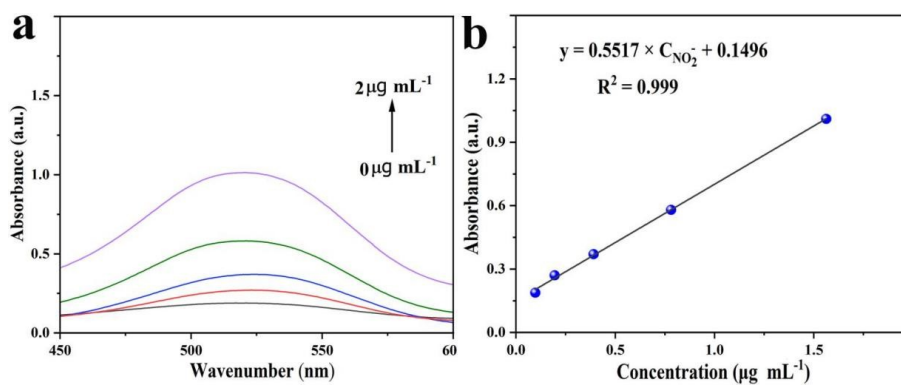


Figure S19. (a) UV-Vis absorption spectra and (b) concentration-absorbance curve of NO_2^- solution with a series of standard concentrations.

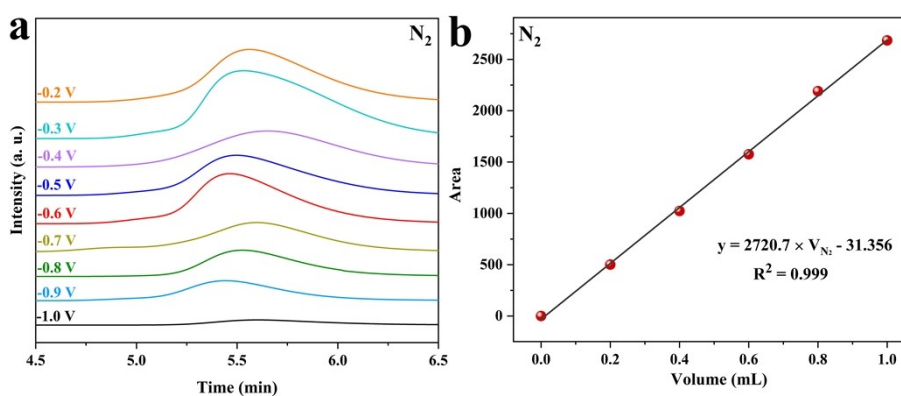


Figure S20. (a) The N_2 spectra measured by GC and (b) N_2 working curve.

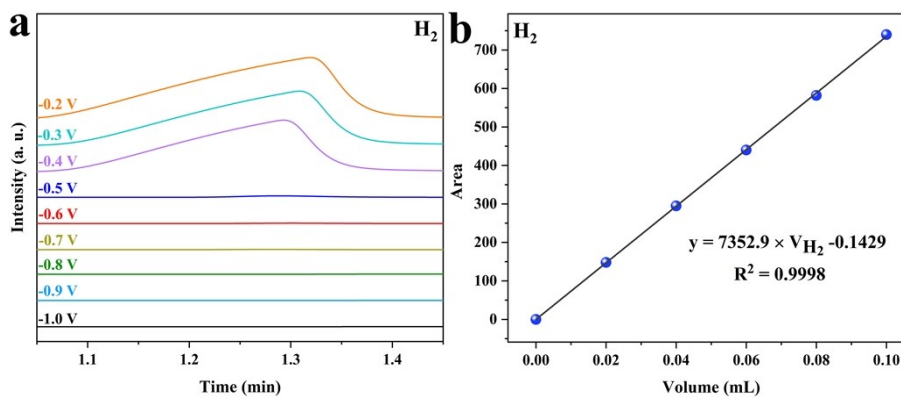


Figure S21. (a) The H_2 spectra measured by GC and (b) H_2 working curve.

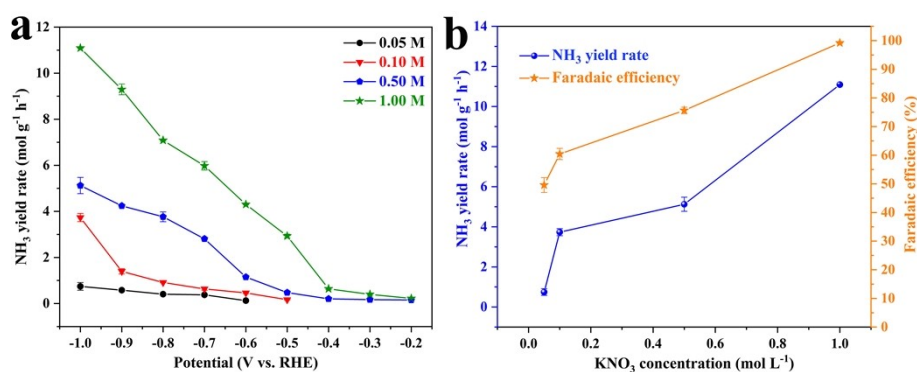


Figure S22. (a) Ammonia yields corresponding to different potassium nitrate concentrations; (b) Ammonia production rates and Faradaic efficiencies corresponding to different potassium nitrate concentrations at -1.0 V.

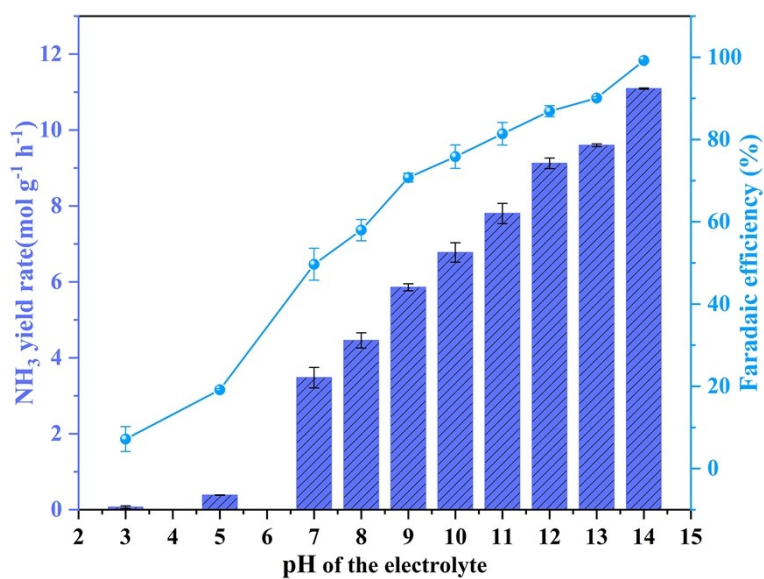


Figure S23. NH_3 yield rates and their corresponding NO_3^- -to- NH_3 Faradaic efficiencies for MFC-2 at different pH values.

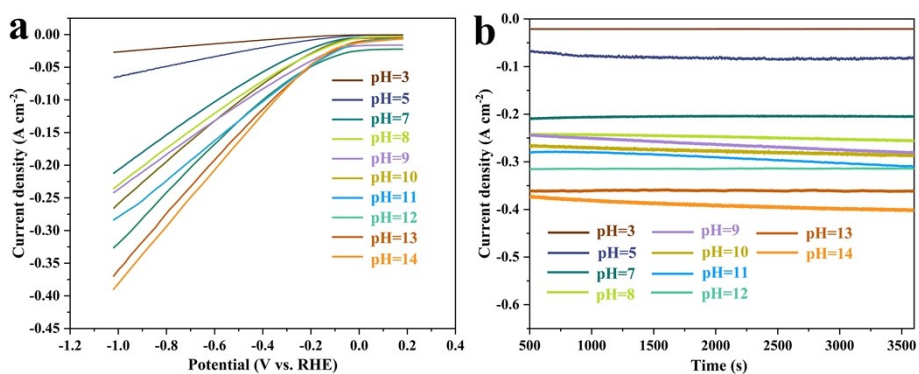


Figure S24. (a) LSV curves and (b) $i-t$ curves under different pH conditions.

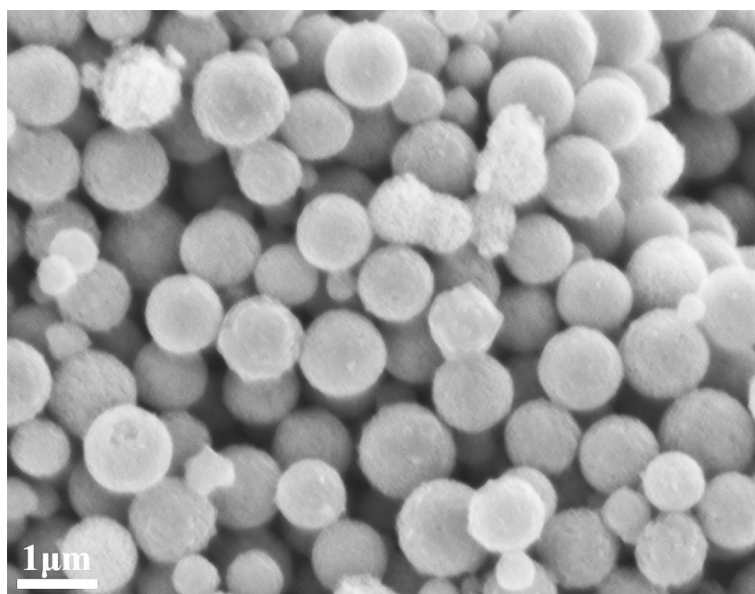


Figure S25. FE-SEM images of MFC-2 after 20 consecutive electrochemical cycles.

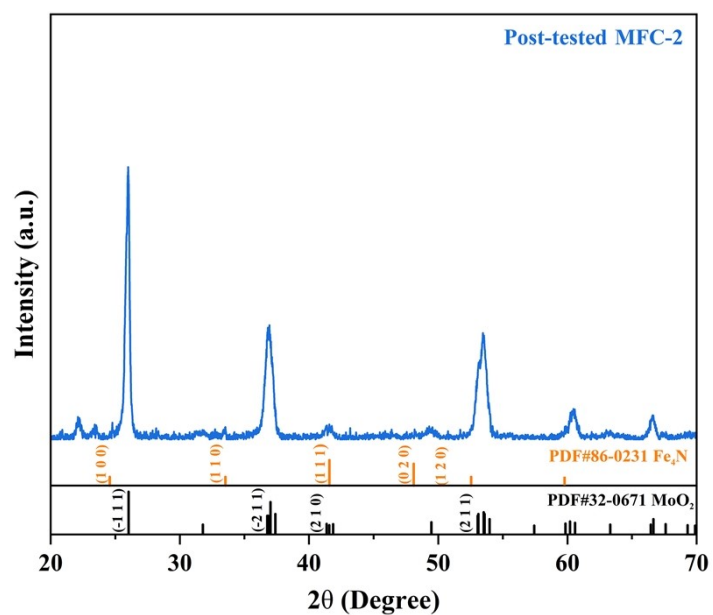


Figure S26. XRD pattern of MFC-2 after 50 hours electrochemical reaction at -1.0 V.

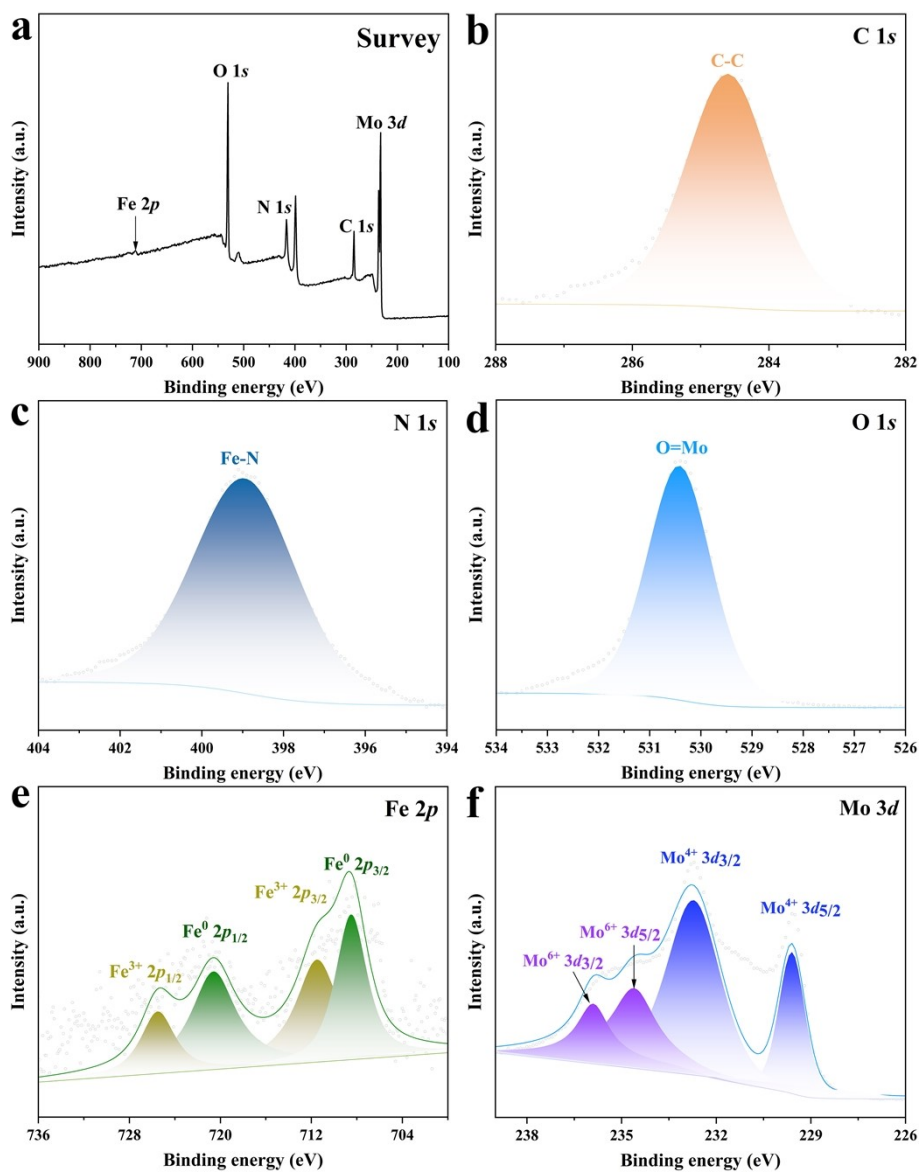


Figure S27. XPS spectra of MFC-2 after 50 hours electrochemical reaction at -1.0 V. (a) Survey (b) C 1s (c) N 1s (d) O 1s (e) Fe 2p and (f) Mo 3d.

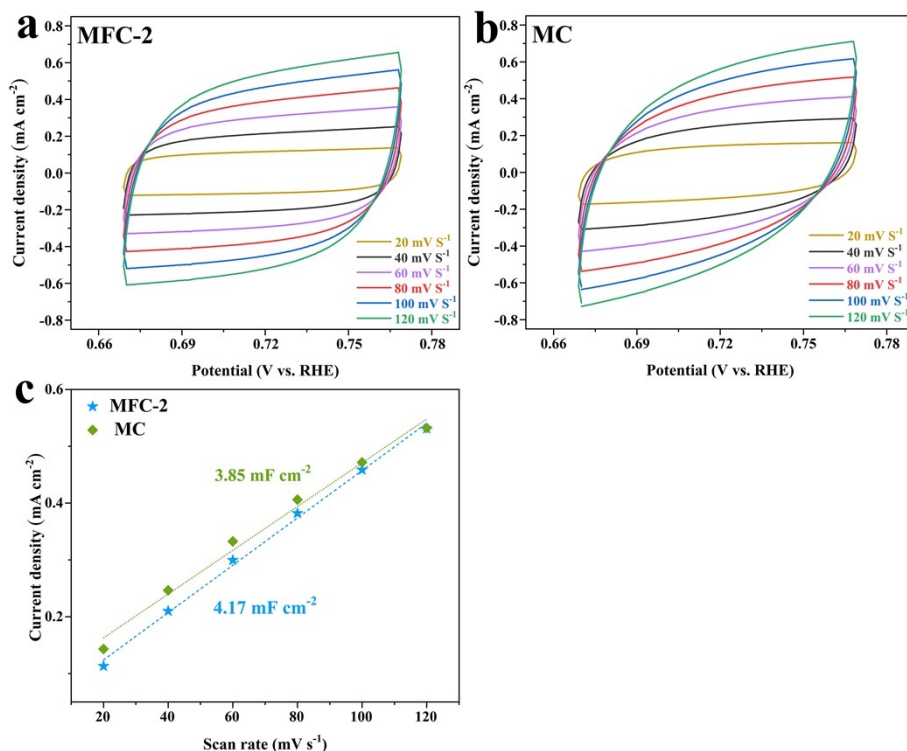


Figure S28. Cyclic voltammetry curves recorded at different scan rates (20–120 mV s^{-1}): (a) MFC-2, (b) MC. (c) Capacitive current densities for MFC-2 and MC samples derived from CV curves with different scan rates.

Estimate the C_{dl} value of the double layer capacitance from the cyclic voltammetry curves recorded at different scanning rates, and then calculate the electrochemical active area ECSA of the catalyst. Linear fit the relationship between $\Delta j/2$ and scanning rate at different scanning rates, and the slope obtained is the C_{dl} value.

$$\text{ECSA} = (C_{dl}/C_s) \times (S_A/m) \quad (6)$$

According to the formula (6) calculated the electrochemical active area ECSA ($\text{m}^2 \text{g}^{-1}$), where C_{dl} is the double layer capacitance, C_s is the characteristic capacitance value of the material (the characteristic capacitance value of an ideal smooth oxide is $60 \mu\text{F cm}^{-2}$), S_A is the actual surface area of the electrode (m^2) and m is the mass of the catalyst (g).

Here we assume that the value of C_s is $60 \mu\text{F cm}^{-2}$, the ECSA of MFC-2 and MC are $2.32 \text{ m}^2 \text{g}^{-1}$ and $2.14 \text{ m}^2 \text{g}^{-1}$, respectively.

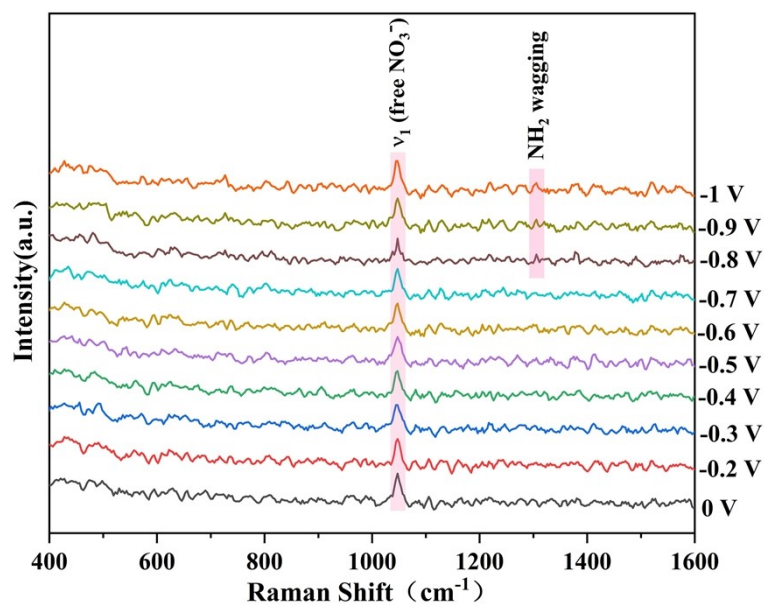


Figure S29. In-situ Raman spectra of MC recorded in electrolyte containing 1 M potassium hydroxide and 1 M potassium nitrate at different potentials from -0.2 V to -1.0 V.

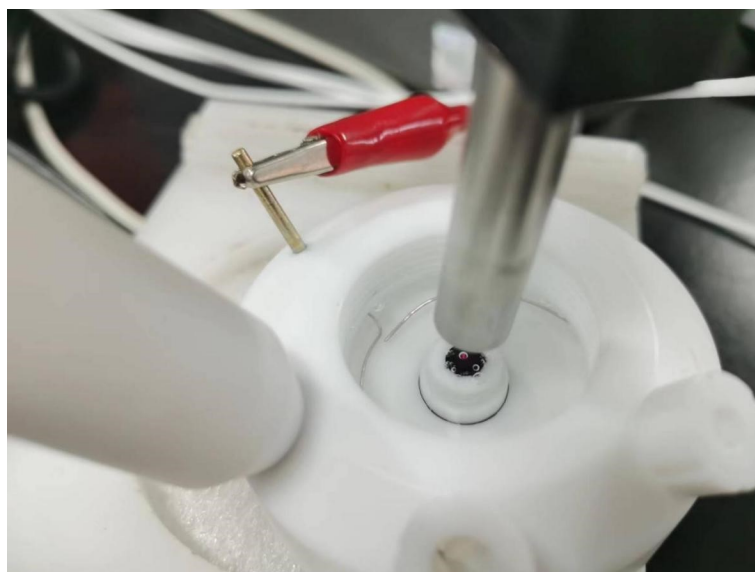


Figure S30. In situ Raman experimental setup diagram.

Table S1. The Fe contents in the final samples are determined by inductively coupled plasma mass spectrometry (ICP-MS).

| Catalyst | Actual content of Fe (wt.%) | Atomic % (Fe) | Atomic % (Mo) |
|----------|-----------------------------|---------------|---------------|
| MC | 0 | 0 | 4.62 |
| MFC-2 | 1.56% | 1.74 | 3.9 |

Table S2. BET areas and pore size results of the samples.

| Sample | BET surface area (m ² g ⁻¹) | Pore diameter (nm) |
|--------|--|--------------------|
| MC | 12.8 | 34.0 |
| MFC-1 | 68.6 | 16.2 |
| MFC-2 | 76.2 | 27.1 |
| MFC-3 | 21.4 | 16.0 |
| MFC-4 | 20.0 | 9.0 |

Table S3. Compare the catalytic performance of MCF-2 with the latest reported catalyst for NO₃RR at the same nitrate concentration.

| Catalyst | Electrolyte | Potential (V vs. RHE) | NH ₃ yield | FE (%) | Reference |
|---------------------------------------|---|-----------------------|---|--------|---|
| MoO ₂ /Fe ₄ N/C | 1 M KOH, 1 M KNO ₃ | -1.0 | 11.10 mol·g ⁻¹ ·h ⁻¹ 1.67 mmol·cm ⁻² ·h ⁻¹ | 99.3 | This work |
| CuPd Nanocube | 1 M KOH, 1 M KNO ₃ | -0.6 | 6.25 mol·g ⁻¹ ·h ⁻¹ | 92.5 | <i>Nat. Commun.</i> , 2022, 13, 2338. ⁵ |
| CoO NC/Graphene | 1 M KOH, 1 M KNO ₃ | -0.71 | 25.63 mol·g ⁻¹ ·h ⁻¹ | 99 | <i>Adv. Energy Mater.</i> , 2023, 13, 2204236. ⁶ |
| CoP NAs/CFC | 1 M NaOH, 1 M NO ₃ ⁻ | -0.3 | 0.596 mol·g ⁻¹ ·h ⁻¹ | ~100 | <i>Energy Environ. Sci.</i> , 2022, 15, 760-770. ⁷ |
| ox-LIG | 1 M NaNO ₃ | -0.93 | 0.168 mmol·cm ⁻² ·h ⁻¹ | 96.4 | <i>Adv. Mater.</i> , 2023, 35, e2211856. ⁸ |
| Strained Ru nanoclusters | 1 M KOH, 1 M KNO ₃ | -0.8 | 5.56 mol·g ⁻¹ ·h ⁻¹ | 96 | <i>J. Am. Chem. Soc.</i> , 2020, 142, 7036-7046. ⁹ |
| Ir nanotubes | 0.1 M HClO ₄ , | 0.06 | 0.0542 mol·g ⁻¹ ·h ⁻¹ | 84.7 | <i>ACS Appl. Mater.</i> |

| | | | | | |
|--|--|-------------|--|-------------|--|
| | 1 M NaNO ₃ | | | | <i>Interfaces</i> , 2020, 12, 14064–14070. ¹⁰ |
| GdSA-D-NiO400 | 1 M KOH, 1 M KNO ₃ | -0.1 | 0.0369 mol·g ⁻¹ ·h ⁻¹ | 97.00 | <i>ACS Nano</i> , 2022, 16, 15297–15309. ¹¹ |
| Cu SACs | 1 M KOH, 1 M KNO ₃ | -1.0 | 13.8 mol·g ⁻¹ ·h ⁻¹ | 95.5 | <i>ChemSusChem</i> , 2022, 15, e202200231. ⁴ |
| MoO₂/Fe₄N/C | 0.1 M KOH, 0.1 M KNO₃ | -1.0 | 3.86 mol·g⁻¹·h⁻¹ 0.58 mmol·cm⁻²·h⁻¹ | 74.4 | This work |
| Cu-N-C | 1 M KOH, 0.1 M KNO ₃ | -1.0 | 12.5 mol·g ⁻¹ ·h ⁻¹ | 84.7 | <i>J. Am. Chem. Soc.</i> , 2022, 144, 12062–12071. ¹² |
| Fe-PPy | 0.1 M KOH, 0.1 M KNO ₃ | -0.7 | 0.714 mol·g ⁻¹ ·h ⁻¹ | ~100 | <i>Energy Environ. Sci.</i> , 2021, 14, 3522–3531. ¹³ |
| In-S-G | 1 M KOH, 0.1 M KNO ₃ | -0.5 | 0.22 mol·g ⁻¹ ·h ⁻¹ | 75 | <i>Chem. Eng. J.</i> , 2021, 426, 134641. ¹⁴ |
| Fe ₃ O ₄ @TiO ₂ /TP | 0.1 M PBS 0.1 M NaNO ₃ | -0.9 | 0.496 mmol·cm ⁻² ·h ⁻¹ | 88.4 | <i>Inorg. Chem.</i> , 2023, 62, 25–29. ¹⁵ |
| Cu@C | 1 M KOH, 0.1 M KNO ₃ | -0.7 | 0.0276 mol·g ⁻¹ ·h ⁻¹ | 72 | <i>Adv. Mater.</i> , 2022, 34, e2204306. ¹⁶ |
| RuOx/Pd | 1 M KOH, 0.1 M KNO ₃ | -0.5 | 1.38 mmol·cm ⁻² ·h ⁻¹ | 98.6 | <i>ACS Nano</i> , 2023, 17, 1081–1090. ¹⁷ |
| Ru-CuNW | 1 M KOH, 0.1 M NO ₃ ⁻ | -0.099 | 4.5 mmol·cm ⁻² ·h ⁻¹ | 95.6 | <i>Nat. Nanotechnol.</i> , 2022, 17, 759–767. ¹⁸ |
| Fe SACs | 0.1 M KOH, 0.1 M KNO ₃ | -0.85 | 0.46 mmol·cm ⁻² ·h ⁻¹ | 69 | <i>Nat. Commun.</i> , 2021, 12, 2870. ¹⁹ |
| Cu-N ₄ | 0.1 M KOH, 0.1 M KNO ₃ | -1.0 | 0.735 mol·g ⁻¹ ·h ⁻¹ | 84.7 | <i>J. Am. Chem. Soc.</i> , 2022, 144, 12062–12071. ¹² |

References

1. W. He, J. Zhang, S. Dieckhofer, S. Varhade, A. C. Brix, A. Lielpetere, S. Seisel, J. R. C. Junqueira and W. Schuhmann, *Nat Commun*, 2022, **13**, 1129.
2. T. Hu, M. Wang, C. Guo and C. M. Li, *Journal of Materials Chemistry A*, 2022, **10**, 8923–8931.
3. F. Rehman, S. Kwon, C. B. Musgrave, M. Tamtaji, W. A. Goddard and Z. Luo, *Nano Energy*, 2022, **103**.
4. M. Xu, Q. Xie, D. Duan, Y. Zhang, Y. Zhou, H. Zhou, X. Li, Y. Wang, P. Gao and W. Ye, *ChemSusChem*, 2022, **15**, e202200231.
5. Q. Gao, H. S. Pillai, Y. Huang, S. Liu, Q. Mu, X. Han, Z. Yan, H. Zhou, Q. He, H. Xin and H. Zhu, *Nat Commun*, 2022, **13**, 2338.
6. N. C. Kani, N. H. L. Nguyen, K. Markel, R. R. Bhawnani, B. Shindel, K. Sharma, S. Kim, V. P. Dravid, V. Berry, J. A. Gauthier and M. R. Singh, *Advanced Energy Materials*, 2023, **13**.
7. S. Ye, Z. Chen, G. Zhang, W. Chen, C. Peng, X. Yang, L. Zheng, Y. Li, X. Ren, H. Cao, D. Xue, J. Qiu, Q. Zhang and J. Liu, *Energy & Environmental Science*, 2022, **15**, 760–770.
8. L. Huang, L. Cheng, T. Ma, J. J. Zhang, H. Wu, J. Su, Y. Song, H. Zhu, Q. Liu, M. Zhu, Z. Zeng, Q. He, M. K. Tse, D. T. Yang, B. I. Yakobson, B. Z. Tang, Y. Ren and R. Ye, *Adv Mater*, 2023, **35**, e2211856.
9. J. Li, G. Zhan, J. Yang, F. Quan, C. Mao, Y. Liu, B. Wang, F. Lei, L. Li, A. W. M. Chan, L. Xu, Y. Shi, Y. Du, W. Hao, P. K. Wong, J. Wang, S. X. Dou, L. Zhang and J. C. Yu, *J Am Chem Soc*, 2020, **142**, 7036–7046.
10. J. Y. Zhu, Q. Xue, Y. Y. Xue, Y. Ding, F. M. Li, P. Jin, P. Chen and Y. Chen, *ACS Appl Mater Interfaces*, 2020, **12**, 14064–14070.
11. A. Kumar, J. Lee, M. G. Kim, B. Debnath, X. Liu, Y. Hwang, Y. Wang, X. Shao, A. R. Jadhav, Y. Liu, H. Tuysuz and H. Lee, *ACS Nano*, 2022, **16**, 15297–15309.
12. J. Yang, H. Qi, A. Li, X. Liu, X. Yang, S. Zhang, Q. Zhao, Q. Jiang, Y. Su, L. Zhang, J. F. Li, Z. Q. Tian, W. Liu, A. Wang and T. Zhang, *J Am Chem Soc*, 2022, **144**, 12062–12071.
13. P. Li, Z. Jin, Z. Fang and G. Yu, *Energy & Environmental Science*, 2021, **14**, 3522–3531.
14. F. Lei, W. Xu, J. Yu, K. Li, J. Xie, P. Hao, G. Cui and B. Tang, *Chemical Engineering Journal*, 2021, **426**.
15. X. He, J. Li, R. Li, D. Zhao, L. Zhang, X. Ji, X. Fan, J. Chen, Y. Wang, Y. Luo, D. Zheng, L. Xie, S. Sun, Z. Cai, Q. Liu, K. Ma and X. Sun, *Inorg Chem*, 2023, **62**, 25–29.
16. Z. Song, Y. Liu, Y. Zhong, Q. Guo, J. Zeng and Z. Geng, *Adv Mater*, 2022, **34**, e2204306.
17. X. Li, P. Shen, X. Li, D. Ma and K. Chu, *ACS Nano*, 2023, DOI: 10.1021/acsnano.2c07911.
18. F. Y. Chen, Z. Y. Wu, S. Gupta, D. J. Rivera, S. V. Lamberts, S. Pecaut, J. Y. T. Kim, P. Zhu, Y. Z. Finfrock, D. M. Meira, G. King, G. Gao, W. Xu, D. A. Cullen, H. Zhou, Y. Han, D. E. Perea, C. L. Muhich and H. Wang, *Nat Nanotechnol*, 2022, **17**, 759–767.
19. Z. Y. Wu, M. Karamad, X. Yong, Q. Huang, D. A. Cullen, P. Zhu, C. Xia, Q. Xiao, M. Shakouri, F. Y. Chen, J. Y. T. Kim, Y. Xia, K. Heck, Y. Hu, M. S. Wong, Q. Li, I. Gates, S. Siahrostami and H. Wang, *Nat Commun*, 2021, **12**, 2870.